

Image-Space Gridding for Nonrigid Motion-Corrected MR Image Reconstruction

Kwang Eun Jang^{a,1}, Mario O. Malavé^{a,b}, and Dwight G. Nishimura^a

This manuscript was compiled on January 29, 2025

Motion remains a major challenge in magnetic resonance (MR) imaging, particularly in free-breathing cardiac MR imaging, where data are acquired over multiple heartbeats at varying respiratory phases. We adopt a model-based approach for nonrigid motion correction, addressing two challenges: (a) motion representation and (b) motion estimation. For motion representation, we derive image-space gridding by adapting the nonuniform fast Fourier transform (NUFFT) to represent and compute nonrigid motion, which provides an exact forward-adjoint pair of linear operators. We then introduce nonrigid SENSE operators that incorporate nonrigid motion into the multi-coil MR acquisition model. For motion estimation, we employ both low-resolution 3D image-based navigators (iNAVs) and high-resolution 3D self-navigating image-based navigators (self-iNAVs). During each heartbeat, data are acquired along two types of non-Cartesian trajectories: a subset of a high-resolution trajectory that sparsely covers 3D k-space, followed by a full low-resolution trajectory. We reconstruct 3D iNAVs for each heartbeat using the full low-resolution data, which are then used to estimate bulk motion and identify the respiratory phase of each heartbeat. By combining data from multiple heartbeats within the same respiratory phase, we reconstruct high-resolution 3D self-iNAVs, allowing estimation of nonrigid respiratory motion. For each respiratory phase, we construct the nonrigid SENSE operator, reformulating the nonrigid motion-corrected reconstruction as a standard regularized inverse problem. In a preliminary study, the proposed method enhanced sharpness of the coronary arteries and improved image quality in non-cardiac regions, outperforming translational motion-corrected reconstruction.

Nonrigid Motion Correction | Free-breathing Cardiac MRI | Gridding

Magnetic resonance (MR) imaging scans generally consist of multiple repetitions of pulse sequences, with each repetition typically lasting from a few milliseconds to several hundred milliseconds. Since movement during this scan period introduces inconsistencies in k-space, often manifesting as ghosting or blurring in image-space, motion remains a major challenge in MR imaging.

We adopt a model-based approach (1) for nonrigid motion correction, formulating an optimization problem that accounts for subject motion and solving it using an iterative solver. This approach involves two primary challenges: (a) motion representation and (b) motion estimation. Motion representation in the model should meet three key requirements. First, it should describe a wide range of motion. Second, its adjoint operation should also be available. Third, it should be computable within a reasonable amount of time, as both the forward and adjoint operations are repeatedly executed within the iterative solver. Motion estimation should have minimal impact on data acquisition while providing sufficient accuracy.

For motion representation, we derive image-space gridding by adapting the nonuniform fast Fourier transform (NUFFT) (2–5) to represent and compute nonrigid motion. Since the proposed linear operators form an exact forward-adjoint pair that can be efficiently implemented on graphics processing units (GPUs) to accelerate computations (6), they are well-suited for iterative reconstructions. Using image-space gridding, we introduce a new linear operator, termed the nonrigid SENSE operator, by preceding the conventional SENSE operator (7) with the forward image-space gridding operator. The nonrigid SENSE operator incorporates the nonrigid transformation of the object into the multi-coil MR acquisition model. By stacking multiple nonrigid SENSE operators corresponding to different transformations of the object, we formulate a linear equation that models the state transitions of the object during the prolonged MR scan.

For motion estimation, we present a method that employs both low-resolution 3D image-based navigators (iNAVs) (8, 9) and high-resolution 3D self-navigating image-based navigators (self-iNAVs) (10), with a primary focus on addressing respiratory motion in free-breathing coronary MR angiography (8, 9, 11–13).

Significance Statement

Motion remains a major challenge in magnetic resonance imaging, particularly in free-breathing cardiac imaging, where data are acquired over multiple heartbeats. Here, we derive image-space gridding by adapting the nonuniform fast Fourier transform (NUFFT) to represent and compute nonrigid motion. Additionally, we present a method that employs both low-resolution 3D image-based navigators and high-resolution 3D self-navigating image-based navigators to estimate translational and nonrigid motion, respectively. Using image-space gridding and the proposed motion estimation scheme, we concisely reformulate the nonrigid motion correction problem as a standard regularized inverse problem. This work could be particularly beneficial for patients unable to hold their breath during cardiac MR scans.

Author affiliations: ^aMagnetic Resonance Systems Research Lab (MRSRL), Department of Electrical Engineering, Stanford University; ^bCurrently affiliated with Apple Inc.

K.E.J. developed the theoretical framework, implemented the algorithm, analyzed the data, and wrote the manuscript. M.O.M. conducted in-vivo experiments. D.G.N. supervised the project and revised the manuscript. All authors discussed the results and contributed to the final version of the manuscript.

¹To whom correspondence should be addressed. E-mail: kejang@stanford.edu

During each heartbeat, data are acquired along two types of non-Cartesian trajectories: a subset of a high-resolution trajectory that sparsely covers 3D k-space, followed by a full low-resolution trajectory. We reconstruct 3D iNAV for each heartbeat using data near the k-space origin, which are then used to estimate bulk motion and identify the respiratory phase of each heartbeat. Since the high-resolution data associated with each heartbeat are distributed across 3D k-space, binning datasets within the same respiratory phase enables the reconstruction of a set of high-resolution 3D self-iNAV across the respiratory cycle. This approach allows capturing nonrigid respiratory motion using a relatively short low-resolution iNAV acquisition during each heartbeat.

The process of nonrigid motion-corrected reconstruction is summarized as follows: A nonrigid image registration method is applied across the 3D self-iNAV to obtain displacement fields (14, 15) with respect to a reference respiratory phase. Using the estimated displacement fields, the proposed nonrigid SENSE operators are constructed for each respiratory phase, incorporating nonrigid motion across multiple heartbeats into the MR acquisition model. In this way, we reformulate the nonrigid motion-corrected reconstruction as a standard regularized inverse problem. In a preliminary study, we show that the proposed method enhances voxel depiction and improves image quality in non-cardiac regions, outperforming translational motion-corrected reconstruction.

Notations

We use $[\cdot]$ and (\cdot) to describe functions or data on Cartesian and non-Cartesian grids, respectively. For example, $M(k_x)$ represents k-space data along a non-Cartesian trajectory, while $m[x]$ denotes the image to be reconstructed on a Cartesian grid. We utilize $\{\cdot\}$ to denote the application of operators. Our symbols for gridding subtly adapt notations in Beatty et al. (4). Table 1 summarizes the notations used in this paper.

Image-based Gridding

We would like to clarify the term “gridding” as used in this paper. In the MR imaging context, “gridding” denotes a specific type of NUFFT; it transforms nonuniform k-space samples to an image on a Cartesian grid (Type-1 NUFFT (2, 3, 5)). To avoid confusion, we label this Type-1 NUFFT as “k-space gridding.” Similarly, the Type-2 NUFFT is termed “inverse k-space gridding,” which generates k-space data on a non-Cartesian grid from an image on a Cartesian grid.

k-space Gridding. 1D k-space gridding is expressed as (4):

$$m[x] = \mathcal{F}^H \left\{ (M(k_x) * C(k_x)) \cdot \text{III}[Gk_x] \right\} [x] \cdot \left(\frac{1}{c[x]} \right). \quad [1]$$

We term the operations within the inverse Fourier transform bracket as the “Projection Core.” Within the Projection Core, non-Cartesian k-space data are convolved with an interpolation kernel, $C(k_x)$, and then sampled on an oversampled Cartesian grid. As depicted in Fig. 1(a), this operation can be visualized as a projection onto a Cartesian grid, with the projection’s extent being determined by the width of the kernel.

Table 1. Notations

Symbol	Definition
x	Image location
k_x	K-space location
N	Number of pixels
G	Number of sample locations on an oversampled grid
$M(k_x)$	Sampled, density corrected k-space data
$\text{III}(x)$	Comb function, $\text{III}(x) = \sum_i \delta(x - i)$
$c(x)$	Interpolation kernel function in image-space
$C(k_x)$	Interpolation kernel function in k-space
$m[x]$	Image to be reconstructed at the reference phase
$m_j[x]$	Warped image at the j -th phase
$\mathcal{T}_j\{\cdot\}$	Nonrigid transform that warps $m[x]$ to $m_j[x]$
$\mathcal{T}_j^H\{\cdot\}$	Adjoint of $\mathcal{T}_j\{\cdot\}$
$\mathcal{F}\{\cdot\}$	Fourier transform
$\mathcal{F}^H\{\cdot\}$	Inverse Fourier transform
$\mathcal{Z}\{\cdot\}$	Zero-padding
$\mathcal{Z}^H\{\cdot\}$	Undo zero-padding (cropping)
$\mathcal{S}\{\cdot\}$	Multiplying a coil sensitivity map
$\mathcal{P}^{(k)}\{\cdot\}$	Projection Core in k-space
$\mathcal{P}^{(i)}\{\cdot\}$	Projection Core in image-space
$\mathcal{B}^{(k)}\{\cdot\}$	Backprojection Core in k-space
$\mathcal{B}^{(i)}\{\cdot\}$	Backprojection Core in image-space
iNAV	image-based navigator
self-iNAV	self-navigating image-based navigator

The implementation of Eq. (1) is outlined as:

$$M(k_x) \rightarrow \mathcal{P}^{(k)} \rightarrow \mathcal{F}^H \rightarrow \mathcal{Z}^H \rightarrow \left[\frac{1}{c[x]} \right] \rightarrow m[x]. \quad [2]$$

The weighting operation $\left[\frac{1}{c[x]} \right]$ is often referred to as deapodization or preemptive emphasis (4, 16). The adjoint of k-space gridding, commonly known as inverse gridding (4, 16), is derived by reversing the sequence in Eq. (2):

$$m[x] \rightarrow \left[\frac{1}{c^*[x]} \right] \rightarrow \mathcal{Z} \rightarrow \mathcal{F} \rightarrow \mathcal{B}^{(k)} \rightarrow M(k_x). \quad [3]$$

Here, $\mathcal{B}^{(k)}$ represents the adjoint of the Projection Core. As illustrated in Fig. 1(b), this operation effectively backprojects values on a Cartesian grid to a non-Cartesian point.

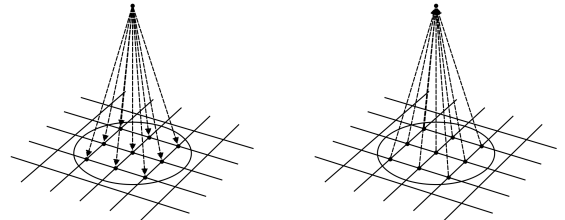


Fig. 1. Conceptual illustrations of Projection and Backprojection Cores. (a) Projection Core: a sample at a non-Cartesian point is projected onto a Cartesian grid. (b) Backprojection Core: samples on a Cartesian grid are backprojected to a non-Cartesian point.

From Eq. (2), we deduce that the k-space gridding operation is essentially a “corrected” version of the Projection

Core. The convolution in k-space corresponds to multiplication in image-space, adding weight in image-space. The deapodization step neutralizes this weight by dividing by the inverse Fourier transform of $C(k_x)$ (4). The k-space gridding operator also includes the \mathcal{Z}^H operation. An oversampled grid is generally employed to suppress aliasing artifacts that are produced by the sampling operation in the Projection Core (4, 16). However, this oversampled grid in k-space leads to an extended field-of-view in image-space. The \mathcal{Z}^H operation recovers the original image extent by cropping the image center.

k-space gridding offers several advantages. It is accurate, especially when employing a well-designed interpolation kernel (3–5, 16). Additionally, optimal kernels and oversampling factors have been extensively studied (3–5). Moreover, the forward and inverse k-space gridding operators form an exact forward-adjoint pair, making them suitable for iterative reconstructions. Last but not least, both operators can be implemented on GPUs for accelerated computations (6).

Displacement Fields. Displacement fields are effective for representing nonrigid transformations (14, 15). Consider two images, m and m_j , and a nonrigid transform, $\mathcal{T}_j\{\cdot\}$, between them:

$$m_j = \mathcal{T}_j\{m\}. \quad [4]$$

With the displacement field, the nonrigid transform is computed by “warping” the input image (14, 15):

$$m_j \begin{bmatrix} x \\ y \\ z \end{bmatrix} = m \begin{pmatrix} x + d_x[x, y, z] \\ y + d_y[x, y, z] \\ z + d_z[x, y, z] \end{pmatrix} = m(\vec{r} + \vec{d}[\vec{r}]), \quad [5]$$

where \vec{d} denotes the displacement field and $\vec{r} = [x, y, z]^T$ represents a voxel location. Various image registration techniques estimate the displacement field from the two given images (15, 17).

From Eq. (5), we infer that the voxel locations of the warped image, m_j , can be regarded as a set of non-Cartesian points on the reference Cartesian grid of m . Therefore, computing $\mathcal{T}_j\{\cdot\}$ is analogous to “inverse gridding,” as it synthesizes “data” at non-Cartesian points from an image on a Cartesian grid. The key differences are that both the operand and the output are in image-space, and the resulting “data” constitutes an image on its own Cartesian grid.

Image-space Gridding. Consider this naive Projection Core for the adjoint of image-space gridding that computes $\mathcal{T}_j^H\{\cdot\}$:

$$(m_j(x) * c(x)) \cdot \text{III}[Nx]. \quad [6]$$

Here, non-Cartesian data are convolved with an interpolation kernel and subsequently sampled onto a Cartesian grid in image-space. However, this operation introduces two problems. Firstly, convolution in image-space leads to additional weightings in k-space. Secondly, sampling in image-space results in aliasing artifacts in k-space.

Similar to k-space gridding, we define the adjoint of image-space gridding by “correcting” these errors:

$$\hat{m}[x] = \mathcal{F}^H \left\{ \mathcal{F} \{ (m_j(x) * c(x)) \cdot \text{III}[Nx] \} \cdot \left(\frac{1}{C[k_x]} \right) \right\} [x], \quad [7]$$

where $\hat{m}[x] = \mathcal{T}_j^H\{m_j[x]\}$. Here, we use the deapodization (preemptive emphasis) step and an oversampled Cartesian

grid to address the additional weighting and the aliasing, respectively. In other words, the same Projection Core is utilized, but it is computed in image-space with subsequent corrections performed in k-space. The process diagram is outlined as follows:

$$m_j[x] \rightarrow \boxed{\mathcal{P}_j^{(i)}} \rightarrow \boxed{\mathcal{F}} \rightarrow \boxed{\mathcal{Z}^H} \rightarrow \boxed{\frac{1}{C[k_x]}} \rightarrow \boxed{\mathcal{F}^H} \rightarrow \hat{m}[x]. \quad [8]$$

With the exception of an additional Fourier transform, this process resembles that of k-space gridding in Eq. (2).

The forward image-space gridding operator that computes $\mathcal{T}\{\cdot\}$ is easily derived by reversing the sequence in Eq. (8):

$$m[x] \rightarrow \boxed{\mathcal{F}} \rightarrow \boxed{\frac{1}{C^*[k_x]}} \rightarrow \boxed{\mathcal{Z}} \rightarrow \boxed{\mathcal{F}^H} \rightarrow \boxed{\mathcal{B}_j^{(i)}} \rightarrow m_j[x], \quad [9]$$

where $m_j[x] = \mathcal{T}_j\{m[x]\}$. With the exception of an additional Fourier transform, this process is analogous to inverse k-space gridding described in Eq. (3).

Image-space gridding inherits key benefits from k-space gridding; its two operators form an exact forward-adjoint pair and can be implemented on GPUs for accelerated computations.

Appendix 1 exemplifies the use of image-space gridding in the context of general nonrigid motion correction, where inverting a nonrigid transform is reformulated as a regularized inverse problem.

Nonrigid SENSE Operators

Here, we propose new operators using image-space gridding, termed nonrigid SENSE operators, to incorporate nonrigid transformations of the object into the multi-coil MR acquisition model. During the prolonged MR scan, we assume that the object exists in several “states,” where the object in each state is modeled by the nonrigid transform of the object at a reference state. In cardiac imaging, these states can correspond to different cardiac and/or respiratory phases. For simplicity, consider two coils, denoted as a and b , and two states of the object, labeled 1 and 2. Let $\mathcal{T}_1\{\cdot\}$ and $\mathcal{T}_2\{\cdot\}$ represent the nonrigid transforms that warp the object x to State-1 and State-2, respectively. Figure 2 provides a schematic representation of this example. The nonrigid SENSE operator for State-1, $\mathcal{A}_1\{\cdot\}$, is constructed by preceding the conventional SENSE operator (7) with the nonrigid transform $\mathcal{T}_1\{\cdot\}$. By vertically stacking both the nonrigid SENSE operators and k-space data, we formulate the data acquisition model, which accounts for the state transitions of the object during the prolonged MR scan, as:

$$\begin{bmatrix} (y_{1,a}) \\ (y_{1,b}) \\ (y_{2,a}) \\ (y_{2,b}) \end{bmatrix} = \begin{bmatrix} y_1 \\ y_2 \end{bmatrix} = \begin{bmatrix} \mathcal{A}_1 \\ \mathcal{A}_2 \end{bmatrix} x, \quad [10]$$

Given that the nonrigid transform is computed using the forward image-space gridding operator, the nonrigid SENSE operator comprises three sequential linear operators: the forward image-space gridding operator, the multiplication by coil sensitivities, and the inverse k-space gridding operator. Its adjoint operator, on the other hand, consists of the adjoints of these three linear operators in reversed order: the forward k-space gridding operator, the multiplication by the conjugate

of coil sensitivities followed by summation, and the adjoint image-space gridding operator. The process diagrams for the forward and adjoint nonrigid SENSE operators are depicted in Fig. 3.

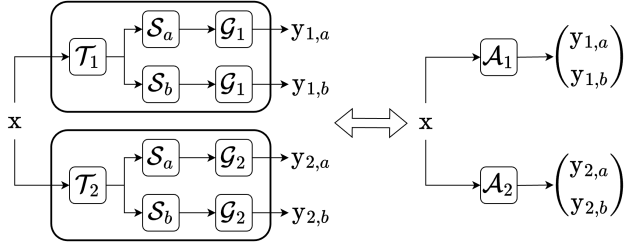


Fig. 2. A schematic representation of nonrigid SENSE operators. For simplicity, only two coils, denoted as a and b , and two states of the object, labeled as 1 and 2, are considered. By vertically stacking both nonrigid SENSE operators and data, we formulate the linear model. \mathcal{T} : nonrigid transform, \mathcal{S} : coil sensitivity, \mathcal{G} : inverse k-space gridding operator, \mathcal{A} : nonrigid SENSE operator, x : target object, y : k-space data.

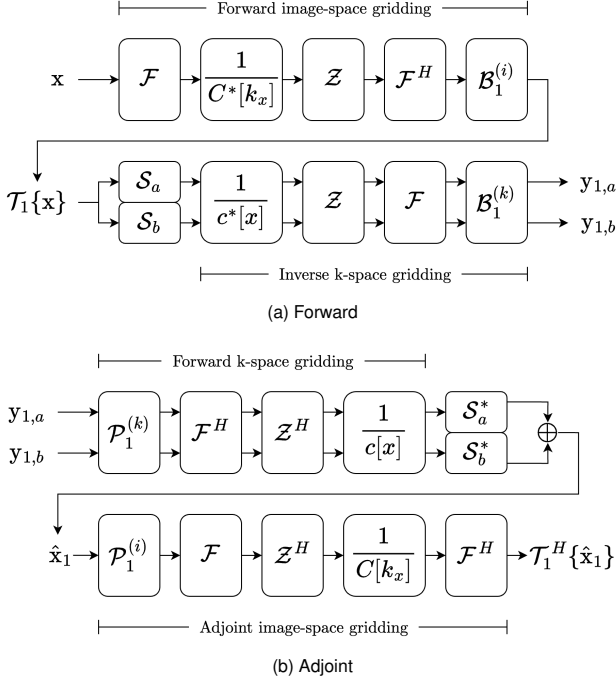


Fig. 3. Process diagrams for (a) forward and (b) adjoint nonrigid SENSE operators. The nonrigid SENSE operator comprises three serial linear operators: the forward image-space gridding operator, the multiplication by coil sensitivities, and the inverse k-space gridding operator. Its adjoint operator consists of the adjoints of the three linear operators in reversed order: forward k-space gridding operator, the multiplication by the conjugate of coil sensitivities followed by summation, and adjoint image-space gridding operator. \hat{x}_1 denotes the output image from the adjoint of the conventional SENSE operator at State-1.

Motion Capturing for Segmented Data Acquisitions

In free-breathing cardiac MR imaging, cardiac triggering is commonly used to synchronize the pulse sequence with the subject's cardiac cycle (16). A subset of data is acquired during each heartbeat under the assumption that cardiac motion remains static during a specific cardiac phase

determined by a trigger delay (16, 18, 19). In our motion capturing scheme for the segmented data acquisition, data are acquired along two types of non-Cartesian trajectories during each heartbeat: a subset of a high-resolution trajectory that sparsely covers 3D k-space, followed by a full low-resolution 3D trajectory.

We reconstruct 3D iNAV (8, 9) using data near the origin of k-space to estimate bulk motion. The process of 3D translational motion correction is summarized as follows: First, one of the 3D iNAVs is selected as a reference. Translational motion for each heartbeat is then estimated by computing correlations between this reference and the other 3D iNAVs (20–22). Finally, the estimated bulk translational motion is corrected by applying linear phase shifts to the k-space data.

At various respiratory phases, the heart may undergo different nonrigid transformations. In other words, data are collected at several distinct states of the imaging object (referred to as subscripts 1 and 2 in Eq. (10)), where these states correspond to respiratory phases in free-breathing cardiac MR imaging. Based on the estimated bulk motion, we identify the respiratory phase of each heartbeat, assuming the location of the heart is closely related to the respiratory phase. Since the high-resolution data from each heartbeat are distributed across 3D k-space, binning these data into discrete respiratory phases enables the reconstruction of high-resolution 3D self-iNAVs (10) for individual respiratory phases. In this way, we capture nonrigid motion using a relatively short low-resolution iNAV acquisition during each heartbeat.

We choose one of these 3D self-iNAVs as a reference and employ an established nonrigid image registration method to calculate displacement fields relative to this reference. Using the estimated displacement fields, we incorporate the nonrigid transform due to respiratory motion into the MR acquisition model through the nonrigid SENSE operator. By stacking pairs of k-space data and their corresponding nonrigid SENSE operators, we formulate the following regularized inverse problem for nonrigid motion-corrected reconstruction:

$$\arg \min_x \left\| \begin{bmatrix} y_0 \\ \vdots \\ y_{N-1} \end{bmatrix} - \begin{bmatrix} \mathcal{A}_0 \\ \vdots \\ \mathcal{A}_{N-1} \end{bmatrix} x \right\|_2^2 + \lambda \|\mathcal{W}x\|_1, \quad [11]$$

where N is the number of respiratory phases, y_i and \mathcal{A}_i denote the multi-coil data and the nonrigid SENSE operator at the i -th respiratory phase, respectively, and \mathcal{W} is a sparsifying operator, such as a wavelet transform (23).

Nonrigid Respiratory Motion Correction

For free-breathing coronary MR angiography, we employ a data acquisition scheme illustrated in Fig. 4 using a balanced steady-state free precession (bSSFP) sequence, similar to prior studies (8, 24, 25). During each R-R interval, high-resolution data are collected along 18 conic interleaves, which are a subset of a 3D Cones phyllotaxis trajectory designed for 1.2-mm isotropic resolution (25). This primary imaging module is followed by a 3D iNAV acquisition using a 3D Cones trajectory designed for 4.4-mm isotropic resolution (24). The following contrast-preparation modules are applied before data acquisition: T2 preparation (26), fat saturation, and sinusoidal bSSFP catalyzation.

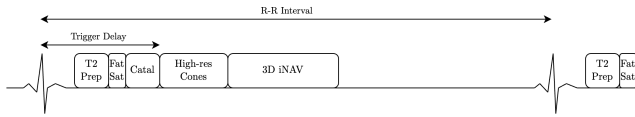


Fig. 4. Imaging modules over an R-R interval for single-phase imaging. T2 Prep: T2 preparation, Fat Sat: fat saturation, Catal: catalyzation, High-res Cones: main data acquisition window, 3D iNAV: 3D image-based navigator.

Figures 5–7 present the preliminary results. Data were acquired on a 1.5T GE Signa scanner using an 8-channel cardiac coil (25) from two healthy subjects.

We identified four respiratory phases using k-means clustering based on the translational motion estimates. The end-expiration phase was selected as the reference for estimating nonrigid motion, as the corresponding cluster showed the least variance in translational motion (27). For nonrigid motion estimation, we employed the symmetric forces diffeomorphic demons algorithm (17), implemented in SimpleITK (20–22). To solve Eq. (11), we used the Wavelet-FISTA algorithm (28).

To validate the measured nonrigid motion, we overlaid the reference and one of the non-reference 3D self-iNAVs in purple and green, respectively, as shown in the middle and rightmost columns of Fig. 5 (27). With this color scheme, well-aligned areas appear gray due to the even mixture of red, blue, and green, while colored pixels highlight discrepancies between the reference and the non-reference respiratory phase. Figure 5 illustrates the nonrigid transformations of the heart across different respiratory phases, demonstrating the potential benefits of nonrigid motion-corrected reconstruction.

Figures 6 and 7 show reconstructed slices near the left anterior descending artery (LAD) and the right coronary artery (RCA) (27). These results demonstrate that the proposed method not only enhances sharpness near the coronary arteries but also improves image quality in non-cardiac regions, outperforming translational motion-corrected reconstruction (27).

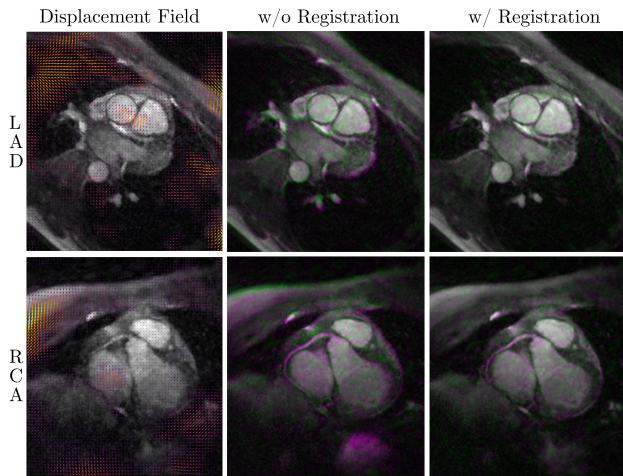


Fig. 5. Left: Estimated displacement fields and 3D self-iNAVs. Middle and right: The reference and one of the non-reference 3D self-iNAVs overlaid in purple and green, respectively, before (middle) and after (right) registration. Gray pixels signify well-aligned areas, while colored pixels highlight discrepancies. This comparison underscores the heart’s nonrigid transformations across different respiratory phases, illustrating the advantages of nonrigid motion-corrected reconstructions.

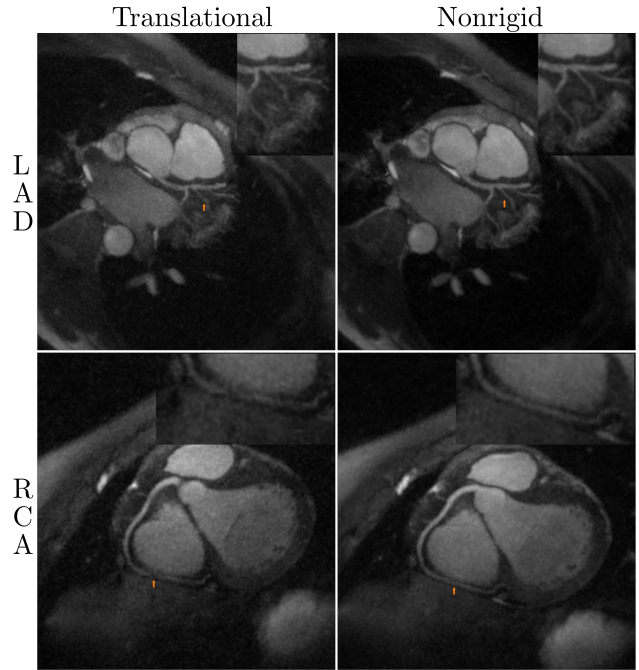


Fig. 6. Reconstructed slices near the LAD and RCA (Subject 1). The proposed method exhibited improved sharpness not only near the coronary arteries (orange arrows) but also in non-cardiac regions compared to 3D translational motion-corrected reconstruction.

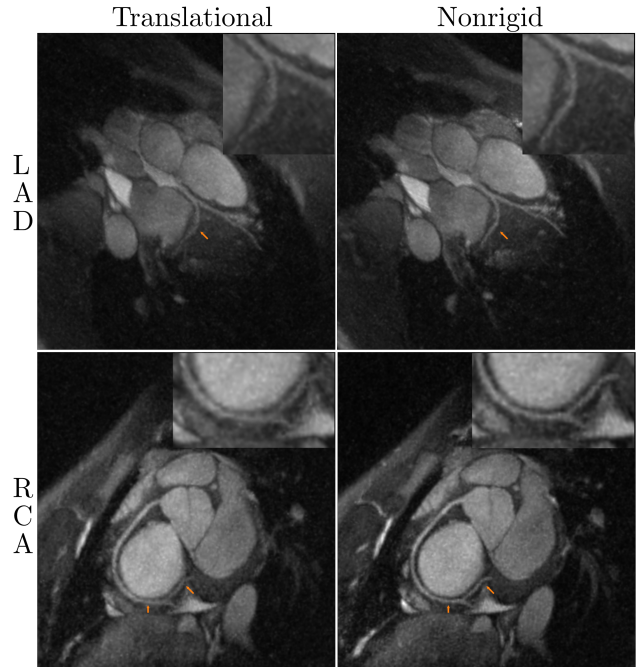


Fig. 7. Reconstructed slices near the LAD and RCA (Subject 2). The proposed method exhibited improved sharpness not only near the coronary arteries (orange arrows) but also in non-cardiac regions compared to 3D translational motion-corrected reconstruction.

Conclusion

We derived a new pair of linear operators, called image-space gridding operators, to compute the forward and adjoint of a

nonrigid transform. We then introduced the nonrigid SENSE operator to integrate the nonrigid transform into the MR acquisition model. By stacking multiple nonrigid SENSE operators for different object states, we formulated an MR acquisition model that accounts for the object’s nonrigid transformations during the prolonged MR scan.

We applied the proposed approach to free-breathing coronary MR angiography. During each heartbeat, two sets of data were acquired: segmented high-resolution data distributed across 3D k-space and low-resolution data. For each heartbeat, the low-resolution 3D iNAV’s were reconstructed to estimate translational motion and identify the respiratory phase. For each respiratory phase, the high-resolution 3D self-iNAV’s were reconstructed using the binned high-resolution data. Nonrigid respiratory motion was estimated by comparing the 3D self-iNAV’s and was subsequently incorporated into the MR acquisition model through the nonrigid SENSE operators. In short, using image-space gridding and the proposed motion estimation process, we reformulated the nonrigid respiratory motion-corrected reconstruction as a standard regularized inverse problem.

In a preliminary study, we demonstrated that the proposed method enhances voxel depiction and improves image quality in non-cardiac regions, outperforming translational motion-corrected reconstruction. Future work will involve a more comprehensive comparison using additional in-vivo datasets.

Acknowledgments

This study was supported by NIH Grant R01 HL127039. Portions of this work were derived from K.E.J.’s doctoral thesis submitted to Stanford University, available at <https://purl.stanford.edu/sc219dv4593>.

Appendix 1: Inverting a Nonrigid Transform

In this Appendix, we consider inverting a nonrigid transform in image-space, exemplifying the use of image-space gridding in the context of general nonrigid motion correction. We have a ground-truth image $p[x, y]$ and a displacement field $\vec{d}[x, y]$, as illustrated in Fig. 8. Let $\mathcal{T}\{\cdot\}$ denote a nonrigid transform defined by the displacement field. Let $q[x, y]$ denote the image after this nonrigid transform:

$$q[x, y] = \mathcal{T}\{p[x, y]\}. \quad [12]$$

The first task is to synthesize $q[x, y]$. We can use `SimpleITK` (20) to apply the nonrigid transform to the ground-truth image $p[x, y]$. Alternatively, we can employ the forward image-space gridding operator to compute $q[x, y]$. The results of both approaches are visually identical, as shown in Fig. 9.

The second task is to recover the original image from $q[x, y]$ assuming that the ground-truth displacement field, $\vec{d}[x, y]$, is available. A naive approach is to negate the image warping by applying the inverted displacement field, $-\vec{d}[x, y]$, to $q[x, y]$. Figure 10(a) shows that inverting a nonrigid transform is not straightforward (29) even if the exact displacement field is given.

Alternatively, we recover $p[x, y]$ by solving this optimization problem:

$$\arg \min_{\mathbf{p}} \|\mathbf{q} - \mathcal{T}\{\mathbf{p}\}\|_2^2 + \lambda \|\mathcal{W}\{\mathbf{p}\}\|_1, \quad [13]$$

where $\mathcal{W}\{\cdot\}$ denotes a sparsifying transform (23) such as a wavelet transform. Using image-space gridding, we construct an exact forward-adjoint pair of linear operators to represent the nonrigid transform and its adjoint, $\mathcal{T}\{\cdot\}$ and $\mathcal{T}^H\{\cdot\}$. Subsequently, we solve Eq. (13) using an iterative solver. For this example, we used 400 iterations of wavelet-FISTA (28) with $\lambda = 10^{-6}$. As shown in Fig. 10(b), this approach provides a more accurate recovery.

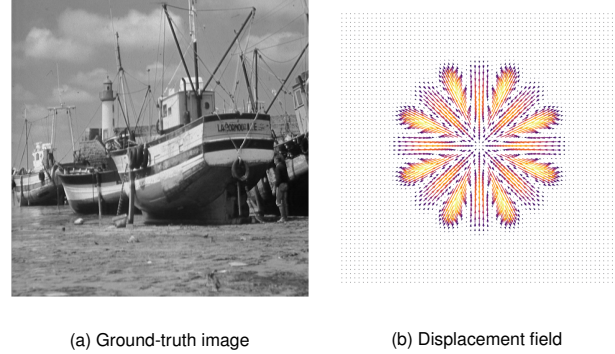


Fig. 8. (a) Ground-truth image and (b) displacement field for the numerical study.

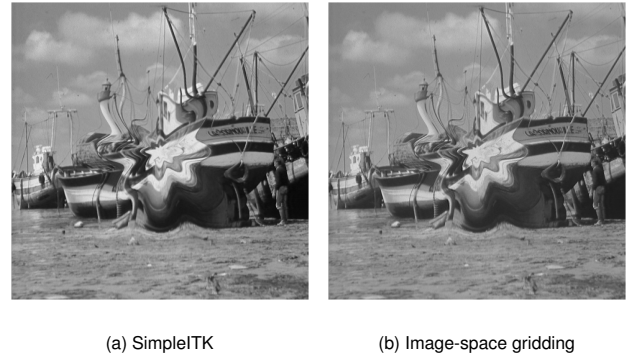


Fig. 9. Transformed images computed using (a) SimpleITK and (b) image-space gridding. The results of both approaches are visually identical.

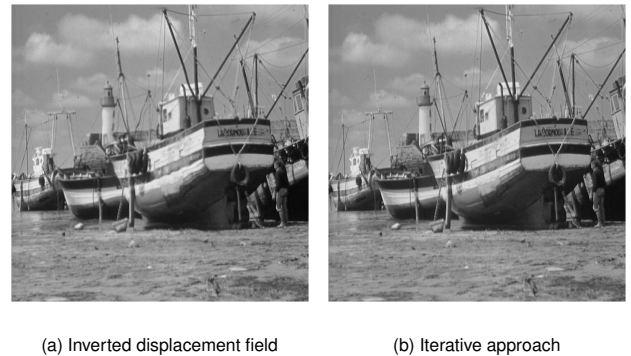


Fig. 10. Recovered images using (a) an inverted displacement field, $(-\vec{d})$, and (b) wavelet-FISTA with image-space gridding, illustrating the challenges in inverting a nonrigid transform. The iterative approach showed a much more accurate recovery.

1. F Odille, PA Vuissoz, PY Marie, J Felblinger, Generalized reconstruction by inversion of coupled systems (GRICS) applied to free-breathing MRI. *Magn. Reson. Medicine* **60**, 146–157 (2008).
2. A Dutt, V Rokhlin, Fast Fourier transforms for nonequispaced data. *SIAM J. on Sci. computing* **14**, 1368–1393 (1993).
3. J Fessler, B Sutton, Nonuniform fast Fourier transforms using min-max interpolation. *IEEE Transactions on Signal Process.* **51**, 560–574 (2003).
4. PJ Beatty, DG Nishimura, JM Pauly, Rapid gridding reconstruction with a minimal oversampling ratio. *IEEE Transactions on Med. Imaging* **24**, 799–808 (2005).
5. JA Fessler, On NUFFT-based gridding for non-Cartesian MRI. *J. Magn. Reson.* **188**, 191–195 (2007).
6. A Gregerson, Implementing fast MRI gridding on GPUs via CUDA. *NVIDIA Whitepaper* (2008).
7. KP Pruessmann, M Weiger, MB Scheidegger, P Boesiger, SENSE: Sensitivity encoding for fast MRI. *Magn. Reson. Medicine* **42**, 952–962 (1999).
8. HH Wu, PT Gurney, BS Hu, DG Nishimura, MV McConnell, Free-breathing multiphase whole-heart coronary MR angiography using image-based navigators and three-dimensional cones imaging. *Magn. Reson. Medicine* **69**, 1083–1093 (2013).
9. NO Addy, et al., 3D image-based navigators for coronary MR angiography. *Magn. Reson. Medicine* **77**, 1874–1883 (2017).
10. J Pang, et al., Whole-heart coronary MRA with 100% respiratory gating efficiency: self-navigated three-dimensional retrospective image-based motion correction (TRIM). *Magn. Reson. Medicine* **71**, 67–74 (2014).
11. L Feng, et al., XD-GRASP: Golden-angle radial MRI with reconstruction of extra motion-state dimensions using compressed sensing. *Magn. Reson. Medicine* **75**, 775–788 (2016).
12. H Bhat, L Ge, S Nielles-Vallespin, S Zuehlsdorff, D Li, 3D radial sampling and 3D affine transform-based respiratory motion correction technique for free-breathing whole-heart coronary MRA with 100% imaging efficiency. *Magn. Reson. Medicine* **65**, 1269–1277 (2011).
13. E Spuentrup, et al., Free-breathing 3D Steady-State Free Precession Coronary MR Angiography with Radial k-Space Sampling: Comparison with Cartesian k-Space Sampling and Cartesian Gradient-Echo Coronary MR Angiography—Pilot Study. *Radiology* **231**, 581–586 (2004).
14. D Rueckert, et al., Nonrigid registration using free-form deformations: application to breast MR images. *IEEE Transactions on Med. Imaging* **18**, 712–721 (1999).
15. J Modersitzki, *Numerical methods for image registration.* (OUP Oxford), (2003).
16. MA Bernstein, KF King, XJ Zhou, *Handbook of MRI pulse sequences.* (Elsevier), (2004).
17. T Vercauteren, X Pennec, A Perchant, N Ayache, et al., Diffeomorphic demons using ITK's finite difference solver hierarchy. *The Insight J.* **1** (2007).
18. MB Hofman, SA Wickline, CH Lorenz, Quantification of in-plane motion of the coronary arteries during the cardiac cycle: implications for acquisition window duration for MR flow quantification. *J. Magn. Reson. Imaging* **8**, 568–576 (1998).
19. Y Wang, et al., Coronary MR angiography: selection of acquisition window of minimal cardiac motion with electrocardiography-triggered navigator cardiac motion prescanning—initial results. *Radiology* **218**, 580–585 (2001).
20. R Beare, B Lowekamp, Z Yaniv, Image Segmentation, Registration and Characterization in R with SimpleITK. *J. Stat. Softw.* **86**, 1–35 (2018).
21. MM McCormick, X Liu, L Ibanez, J Jomier, C Marion, ITK: enabling reproducible research and open science. *Front. Neuroinformatics* **8**, 13 (2014).
22. BC Lowekamp, DT Chen, L Ibáñez, D Blezek, The design of SimpleITK. *Front. Neuroinformatics* **7**, 45 (2013).
23. M Lustig, D Donoho, JM Pauly, Sparse MRI: The application of compressed sensing for rapid MR imaging. *Magn. Reson. Medicine* **58**, 1182–1195 (2007).
24. NO Addy, RR Ingle, HH Wu, BS Hu, DG Nishimura, High-resolution variable-density 3D cones coronary MRA. *Magn. Reson. Medicine* **74** (2015).
25. MO Malavé, et al., Whole-heart coronary MR angiography using a 3D cones phyllotaxis trajectory. *Magn. Reson. Medicine* **81**, 1092–1103 (2019).
26. JH Brittain, et al., Coronary Angiography with Magnetization-Prepared T2 Contrast. *Magn. Reson. Medicine* **33**, 689–696 (1995).
27. KE Jang, DG Nishimura, SS Vasanaawala, Nonrigid Motion-corrected Reconstruction Using Image-space Gridding for Free-breathing Cardiac MRI in *Proceedings of the 29th Annual Meeting of the ISMRM.* (2021).
28. A Beck, M Teboulle, A fast iterative shrinkage-thresholding algorithm for linear inverse problems. *SIAM J. on Imaging Sci.* **2**, 183–202 (2009).
29. M Chen, W Lu, Q Chen, KJ Ruchala, GH Olivera, A simple fixed-point approach to invert a deformation field. *Med. Phys.* **35**, 81–88 (2008).